Chinese Chemical Letters 33 (2022) 4792–4797

Contents lists available at ScienceDirect

Chinese Chemical Letters

journal homepage: www.elsevier.com/locate/cclet

A natural manganese ore as a heterogeneous catalyst to effectively activate peroxymonosulfate to oxidize organic pollutants

Jinchuan Gu[a], Ping Yin[b], Yi Chen[a,*], Honglin Zhu[a], Rui Wang[c]

[a] School of Food and Bioengineering, Civil Engineering and Architecture and Environment, Emergency Science, Xihua University, Chengdu 610039, China
[b] Sichuan Rongxinkai Engineering Design Co., Ltd., Chengdu 610039, China
[c] Faculty of Geosciences and Environmental Engineering, Southwest Jiaotong University, Chengdu 611756, China

ARTICLE INFO

Article history:
Received 14 October 2021
Revised 4 December 2021
Accepted 11 January 2022
Available online 16 January 2022

Keywords:
Transition metal
Heterogeneous catalyst
Natural ore
Orange II
Peroxymonosulfate

ABSTRACT

Heterogeneous transition metal catalysts are indispensable in improving environmental pollution. However, their fabrication is often costly and cumbersome, and they can easily pollute the environment. This study proposed using a natural Gabonese ore (GBO) containing Mn_xO_y and Fe_xO_y as catalysts to degrade orange II (OII) *via* peroxymonosulfate (PMS) activation. The GBO + PMS system exhibited extraordinarily high stability and catalytic activity towards OII elimination (92.2%, 0.0453 min^{-1}). The reactive oxygen species (ROS) generated in the system were identified using radical scavenging tests and electron spin-resonance (ESR) analysis. Singlet oxygen ($^1O_2$) represented the dominant reactive species for OII degradation, while the system presented a lower reaction energy barrier and was effective in a broad pH range (2–10). This work also proposed the activation mechanism for the GBO + PMS system and OII degradation pathways. This study revealed a new approach for exploring inexpensive, eco-friendly, efficient, and stable heterogeneous transition metal catalysts.

Advanced oxidation processes (AOPs) are effective in completely decomposing target organic pollutants in wastewater [1–5]. Sulfate radical ($SO_4^{\bullet-}$)-based AOPs (SR-AOPs) show significant promise for treating the refractory organics in water [6–8] since $SO_4^{\bullet-}$ exhibits a higher standard redox potential (E^0 = 2.5–3.1 V *vs.* 1.8–2.7 V of $^{\bullet}OH$) and a longer half-life period (30–40 μs *vs.* 20 ns of $^{\bullet}OH$) in a wide pH range [6,9–13]. $SO_4^{\bullet-}$ mainly results from persulfate (PS) or peroxymonosulfate (PMS) activation. In addition, it is believed that PMS is more easily dissociated into $SO_4^{\bullet-}$ than PS due to its asymmetric structure and lower bond energy of "O—O" [7,14,15]. Various methods have been developed for PMS stimulation to generate $SO_4^{\bullet-}$, such as heat [16,17], ultrasound [18,19], and ultraviolet (UV) light [20,21]. However, using these methods to activate PMS requires additional energy, which is expensive. Therefore, identifying a simple and economical method for PMS activation is essential.

Heterogeneous catalytic activation is considered promising since the heterogeneous catalyst is easily separated and reused without requiring additional energy [10,22]. Furthermore, transition metals, oxides, and bimetallic oxides are reportedly efficient heterogeneous catalysts for PMS activation since they necessitate less complex system configurations and are more economical for organic pollutant decontamination [6,10]. Although recent studies have shown that cobalt represents the most effective PMS activator [7,23,24], it is expensive and leads to unavoidable, highly toxic leaching. Therefore, it is essential to explore non-cobalt-based heterogeneous catalysts for PMS application during environmental remediation.

The performance of heterogeneous transition metal-based catalysts heavily depends on the nature of the transition metal, the valence state, crystallinity, structure, and surface morphology [1,25]. Due to the natural abundance of multivalent transition metals, iron oxides, and manganese oxides, they are more environmentally friendly than cobalt ions and possibly provide an alternative to cobalt-based catalysts. Mixed metal catalyst loading reportedly improves redox activity and catalytic capacity due to the synergistic redox coupling of different metals and the presence of mixed-valence transition metals [6,10,26]. Consequently, iron-manganese bimetallic oxides have been synthesized to further enhance their catalytic capacity and have exhibited a significantly higher catalytic capacity than monometallic oxides [26–29]. Although considerable advances have been made, challenges remain regarding the fabri-

* Corresponding author.
E-mail address: evechen1@163.com (Y. Chen).

https://doi.org/10.1016/j.cclet.2022.01.029
1001-8417/

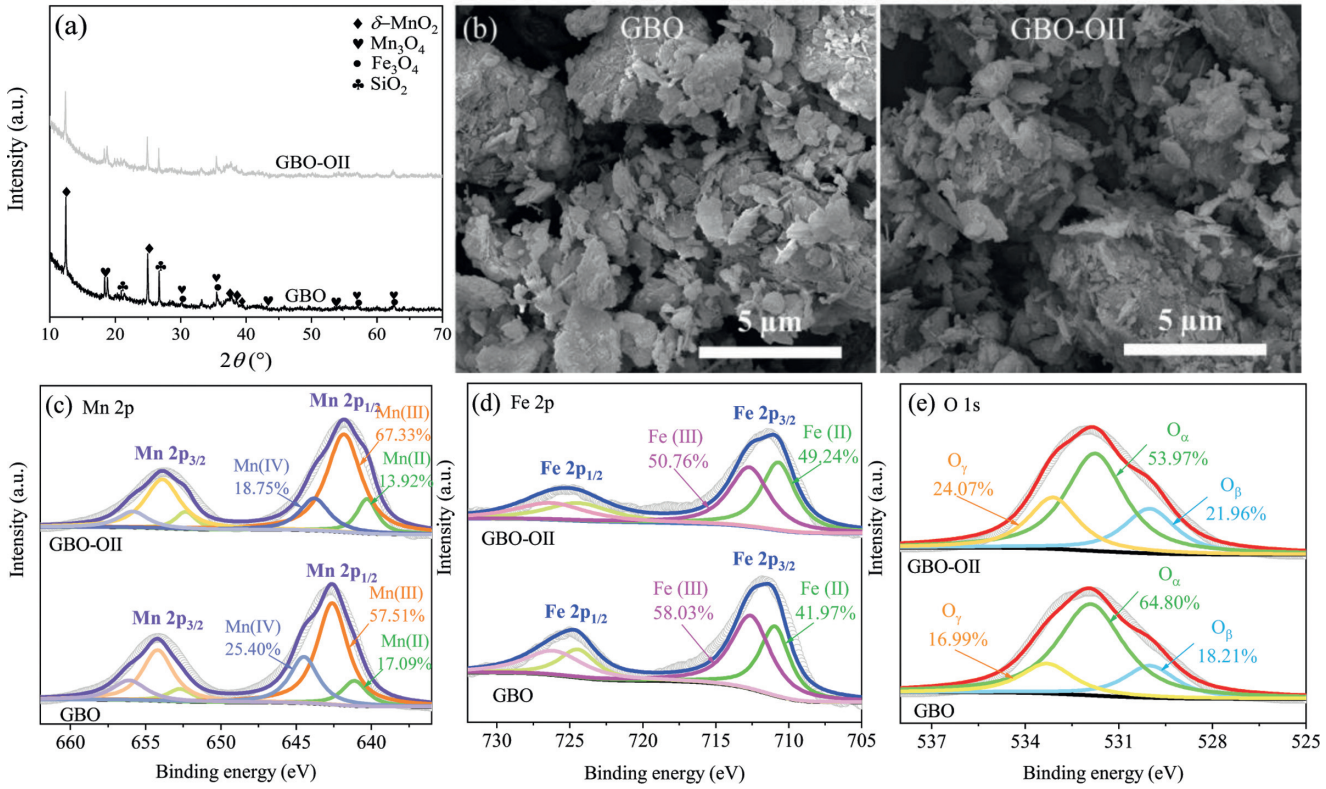

Fig. 1. (a) The XRD patterns and (b) SEM images of the GBO and GBO–OII, and XPS spectra of the GBO catalyst before and after the reaction: (c) Mn 2p, (d) Fe 2p, and (e) O 1s.

cation of iron-manganese bimetallic oxide catalysts. The process is complicated, costly, and can easily cause environmental pollution. Therefore, developing a simple, inexpensive, eco-friendly technique for catalyst synthesis or exploring natural materials exhibiting catalytic bimetallic oxide properties is crucial.

This study proposes a natural manganese ore containing iron and manganese elements as a PMS activation catalyst while evaluating its catalytic capacity and stability. The catalyst is characterized systematically and is employed for PMS decomposition with orange II (OII) as the representative pollutant. A series of catalytic tests are performed to identify the main conditions affecting the catalytic capacity and the main reactive species. Based on the results, a simple mechanism for PMS decomposition and the subsequent degradation and mineralization of OII is proposed.

The X-ray diffraction (XRD) pattern (Fig. 1a) showed that δ-MnO_2 (JCPDS No. 80-1098), Mn_3O_4 (JCPDS No. 13-0162), Fe_3O_4 (JCPDS No. 89-0688), and SiO_2 (JCPDS No. 46-1045) represented the primary GBO phases, while the manganese oxide content was the highest (Fig. S1 in Supporting information). The scanning electron microscopy (SEM) images in Fig. 1b showed that GBO consisted of different-sized particles, appearing as piles of layered structures mainly related to δ-MnO_2 [30,31]. The N_2 adsorption-desorption isotherms of GBO and GBO–OII were type V with H3 hysteresis loops, as depicted in Fig. S2 (Supporting information). The BET surface area (S_{BET}) of GBO was 27.39 m^2/g, and the total pore volume (V_{tot}) was 0.054 cm^3/g (Table S1 in Supporting information), mainly denoting mesoporous characteristics. The XRD pattern, SEM, and textural properties of GBO–OII showed minor changes after catalyzation, indicating that the GBO structure was relatively stable.

Wide scan X-ray photoelectron spectroscopy (XPS) spectra (Fig. S3a in Supporting information) were used to investigate the elemental composition and chemical status of Mn, Fe, and O in the GBO catalyst. This indicated that GBO primarily consisted of O, Mn, Fe, Si, and Al, corresponding to its main elemental composition. The Mn $2p_{3/2}$ spectra in the fresh GBO (Fig. 1c) presented three individual peaks at 641.1 eV, 642.6 eV, and 644.5 eV, which were assigned to Mn(II), Mn(III), and Mn(IV), respectively [1], indicating the polyvalent state of Mn in GBO. The Fe $2p_{3/2}$ peaks (Fig. 1d) at 710.9 eV and 712.6 eV corresponded to Fe(II) and Fe(III), respectively [32–35]. As illustrated in Fig. 1e, the O 1s spectra of the fresh and used GBO were deconvoluted into three components: lattice oxygen (O_β, O^{2-}), surface oxygen (O_α, –OH), and adsorbed oxygen (O_γ, H_2O) at 530.0 eV, 531.9 eV, and 533.3 eV, respectively [7,36,37]. The –OH groups can reportedly provide active sites for PMS bonding [2,37,38]. A reduction of 10.83% was evident in the oxygen content on the GBO surface after the reaction, indicating that –OH was involved in the reaction process, which was also confirmed *via* Fourier transform infrared spectroscopy (FTIR) (Fig. S3b in Supporting information). Furthermore, $-CH_2$ signal peaks at 2989 cm^{-1} and 2901 cm^{-1} were observed on GBO–OII [39], indicating OII decomposition on the GBO surface. In general, the FTIR spectra of GBO changed slightly, indicating the relative stability of the GBO surface properties.

A series of experiments were performed to investigate the catalytic oxidation ability. In all cases, the degradation process of OII followed *pseudo*-first-order kinetics, while the *pseudo*-first-order rate constant (k_{obs}) was acquired *via* the linear regression of ln (C_t/C_0) to time (Eq. 1) [1,40,41].

$$\ln (C_t/C_0) = - k_{obs} \cdot t \quad (1)$$

where t is the reaction time, and C_0 and C_t are the OII concentrations at initial and t time.

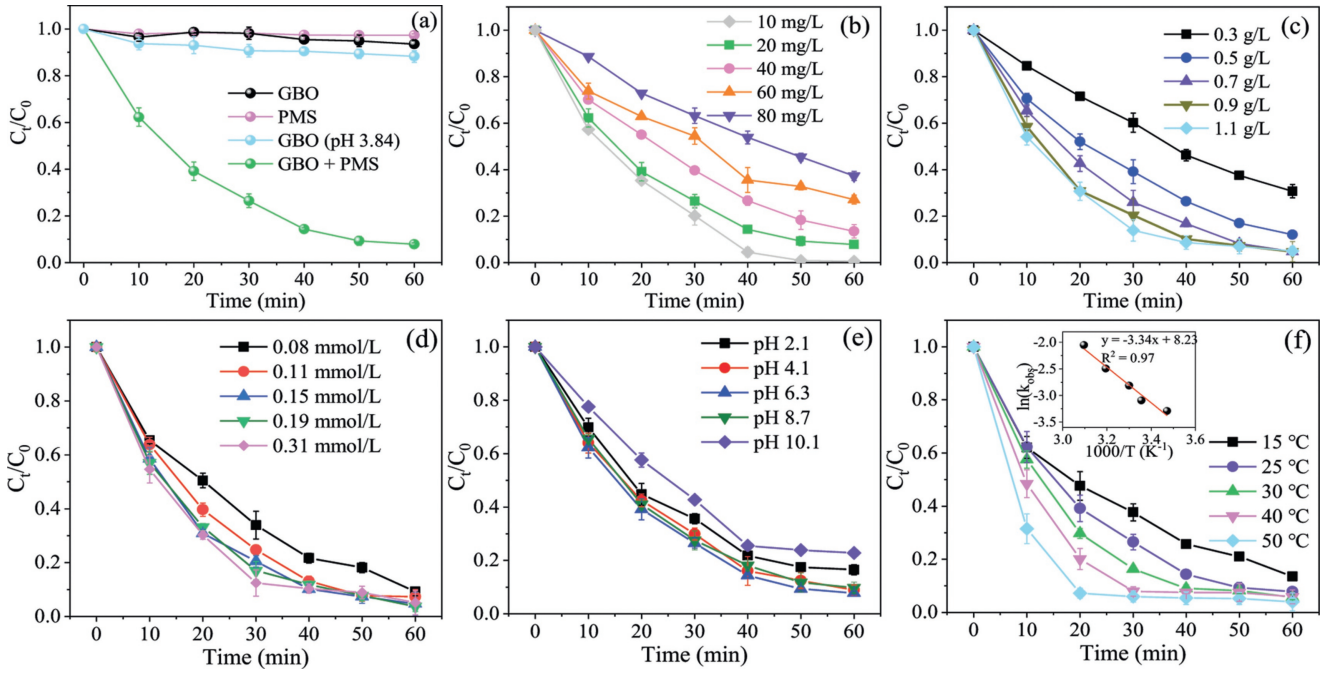

Fig. 2. (a) The degradation of OII in various systems (M_{GBO} = 0.9 g/L). The impact of (b) the initial OII solution concentration (M_{PMS} = 0.14 mmol/L), (c) GBO dosage, (d) PMS dosage (M_{GBO} = 0.9 g/L), (e) initial pH (M_{PMS} = 0.14 mmol/L), and (f) reaction temperature on OII degradation. Conditions: C_0 = 20 mg/L, M_{GBO} = 0.97 g/L, M_{PMS} = 0.15 mmol/L, pH 6.6, T = 25 °C.

The OII removal was evaluated in various aqueous systems, and the results are shown in Fig. 2a. The adsorption of OII on GBO and PMS alone was negligible. It is well known that PMS hydrolysis generates abundant H^+, further influencing the initial pH of the solution [41]. Considering that the pH of the aqueous system changed (about 3.84) after adding PMS, the catalytic oxidation properties of GBO were investigated at a solution pH of 3.84. The OII removal rate in the GBO (pH 3.84) (11.7%) system was noticeably higher than GBO (6.5%) and PMS (2.7%).

GBO (pH 3.84) alone only induced an OII removal of 11.7% in 60 min, while a 92.2% rate was achieved by the GBO + PMS system, exceeding the total of that in the PMS (2.7%) and GBO (pH 3.84) (11.7%) systems, indicating a synergistic effect between PMS and GBO. In addition, the reaction rate constant k_{obs} values were further compared (Fig. S4a in Supporting information). The k_{obs} value of the GBO + PMS system (0.0453 min^{-1}) was 18.88 times and 41.18 times higher than in the GBO (pH 3.84) (0.0024 min^{-1}) and GBO system (0.0011 min^{-1}), respectively. In addition, the catalytic activity of the pure substances in GBO (δ-MnO_2, Mn_3O_4, Fe_3O_4, and SiO_2) was compared in Fig. S5a (Supporting information). The results show that Mn_3O_4 displayed the strongest catalytic activity, while δ-MnO_2 and Fe_3O_4 were weak, and SiO_2 exhibited no activity. However, the removal rate of OII by GBO (92.2%) was substantially higher than Mn_3O_4 (27.0%). These results suggest that GBO displays a significant capacity for PMS activation and OII elimination. Furthermore, GBO demonstrates excellent removal performance involving other dyes in wastewater (Fig. S5b in Supporting information), highlighting its promise for practical application.

The parameters affecting OII oxidation were investigated, including the OII concentration (C_0), GBO dosage (M_{GBO}), PMS dosage (M_{PMS}), initial solution pH, and reaction temperature (T). The OII was completely removed within 60 min at an initial concentration of 10 mg/L (Fig. 2b). As the C_0 increased, the OII removal rate and the reaction rate constant (k_{obs}, Fig. S4b in Supporting information) decreased significantly. In addition, the removal rate and k_{obs} increased in conjunction with M_{GBO} (Fig. 2c). However, at dosages of 0.9 g/L and 1.1 g/L, the respective system k_{obs} were close (Fig. S4c in Supporting information), indicating complete PMS decomposition by the catalyst. It is well known that the PMS concentration significantly affects catalytic reactions. Fig. 2d and Fig. S4d (Supporting information) verify that a high PMS dosage may generally increase the reaction rate. However, it has been proposed that PMS overdosage has a scavenging effect on $SO_4^{\bullet-}$ (Eq. 2), while excessive $SO_4^{\bullet-}$ can also cause a self-scavenging reaction (Eq. 3) [7,42]. Therefore, 0.15 mmol/L M_{PMS} is more appropriate for OII degradation.

$$HSO_5^- + SO_4^{\bullet-} \rightarrow HSO_4^- + SO_5^{\bullet-} \quad (2)$$

$$SO_4^{\bullet-} + SO_4^{\bullet-} \rightarrow S_2O_8^{2-} \quad (3)$$

The solution pH plays a crucial role in the heterogeneous catalytic oxidation process by influencing substrate and oxidant speciation [41,43]. As illustrated in Fig. 2e, the removal of OII was inhibited slightly in acidic and alkaline conditions, with only about 83.5% and 77.16% of OII removed at pH 2.1 and pH 10.1, respectively. In acidic conditions, the high H^+ concentration scavenged $^{\bullet}OH$ and $SO_4^{\bullet-}$, reducing OII degradation (Eqs. 4 and 5) [44–46]. In alkaline conditions, the PMS became unstable, decomposing to sulfate ions (SO_4^{2-}) and oxygen (O_2) (Eq. 6) [44], consequently reducing the OII degradation rate. The GBO + PMS system achieved optimal OII removal at a pH of 6.3, with the removal rate reaching 92.2% at a k_{obs} of 0.0472 min^{-1}. Moreover, the OII removal rate (>91.2%) and k_{obs} (>0.0413 min^{-1}) were relatively high at pH values ranging from 4.1 to 8.7. The broad pH application range indicates that the established GBO + PMS system exhibits significant potential for OII degradation.

$$SO_4^{\bullet-} + H^+ + e^- \rightarrow HSO_4^{\bullet-} \quad (4)$$

$$^{\bullet}OH + H^+ + e^- \rightarrow H_2O \quad (5)$$

$$2HSO_5^- + 2OH^- \rightarrow 2SO_4^{2-} + O_2 + H_2O \quad (6)$$

As shown in Fig. 2f and Fig. S4f (Supporting information), the OII removal and reaction rates increased significantly in conjunction with higher temperatures. The OII removal rate increased from 86.6% to 97.9% as the temperature rose from 15 °C to 50 °C, while the k_{obs} value was rapidly elevated from 0.0372 min^{-1} to 0.1283 min^{-1}, indicating that the GBO activation of PMS was an endothermic reaction. The reaction produced more active sulfate and hydroxyl radicals at high temperatures, improving the OII degradation efficiency [7,47].

The activation energy (E_a) of the OII degradation in the GBO + PMS system was calculated using the Arrhenius equation (Eq. 7), producing a value of 27.77 kJ/mol, significantly exceeding the E_a values in the diffusion-controlled reactions (10–13 kJ/mol) [23,32]. The apparent reaction rate of OII degradation was mainly determined by the intrinsic chemical reaction rate on the GBO surface rather than the mass transfer rate [41,48]. In addition, the E_a value (27.77 kJ/mol) was substantially lower than that previously reported for PMS activation *via* different heterogeneous catalysts (Table S2 in Supporting information). This suggests that GBO with a lower reaction energy barrier can remove pollutants, rendering it promising for practical application.

$$\ln k_{obs} = \ln A - \frac{E_a}{RT} \quad (7)$$

where A is the prefactor, and R is the universal gas constant (8.314 J mol^{-1} K^{-1}).

The effect of the inorganic anions in water on OII removal was also investigated. As shown in Figs. S5c and d (Supporting information), the introduction of Cl^- (0–20 mmol/L) promoted the OII degradation process, while HCO_3^- (0–20 mmol/L) inhibited it. Previous studies have shown that Cl^- can be oxidized by PMS to form HOCl as an additional oxidant for OII degradation [49,50]. HCO_3^- can react with PMS to form fewer active free radicals, leading to the inefficacy of PMS [39]. Therefore, although HCO_3^- influenced the OII degradation rate, the overall degradation efficiency remained >86.0%, indicating that the GBO + PMS system displayed excellent resistance to inorganic ions.

PMS activation can reportedly produce different types of ROS, such as $SO_4^{\bullet-}$, $^{\bullet}OH$, $O_2^{\bullet-}$, and $^1O_2$ [1,32,41]. ROS represents the main factors of OII degradation catalyzed by GBO + PMS. A series of quenching tests were performed to further investigate the key active species in the system. Ethyl alcohol (EtOH) was used as a scavenger for both $SO_4^{\bullet-}$ ($k_2(SO_4^{\bullet-}, EtOH) = 1.6–7.7 \times 10^7$ L mol^{-1} s^{-1}) and $^{\bullet}OH$ ($k_2(^{\bullet}OH, EtOH) = 1.2–2.8 \times 10^9$ L mol^{-1} s^{-1}), while *tert*–butyl alcohol (TBA) was used as an effective quenching agent for $^{\bullet}OH$ ($k_2(^{\bullet}OH, TBA) = 3.8–7.6 \times 10^8$ L mol^{-1} s^{-1}) [7,41,42]. Fig. 3a illustrates that 300 mmol/L EtOH or TBA had a minimal impact on OII oxidation, while 1 mol/L EtOH or TBA enhanced its inhibition. However, about 81.8% (EtOH) and 74.1% (TBA) of OII could be eliminated, implying that only a small amount of $SO_4^{\bullet-}$ and $^{\bullet}OH$ were produced. TBA at 1 mol/L displayed a significantly stronger inhibitive effect on OII degradation than EtOH. This could be attributed to the fact that the higher viscosity of TBA concealed the active sites on the GBO surface, reducing catalytic efficiency [32].

Furfuryl alcohol (FFA) and L-Histamine (L-His) were used to explore the presence of $^1O_2$ ($k_2(^1O_2, FFA) = 1.2 \times 10^8$ L mol^{-1} s^{-1}, $k_2(^1O_2, L\text{-His}) = 3.2 \times 10^7$ L mol^{-1} s^{-1}), while benzoquinone (BQ) was selected for $O_2^{\bullet-}$ ($k_2(O_2^{\bullet-}, BQ) = 0.9–1 \times 10^9$ L mol^{-1} s^{-1}) scavenging [41,51]. According to the results shown in Fig. 3b, BQ had little effect on OII degradation, possibly indicating that $O_2^{\bullet-}$ contributed minimally to the system. Previous studies have shown that BQ can activate PMS and accelerate its decomposition to form $^1O_2$ (Eqs. 8 and 9) [52,53]. Therefore, the inapparent inhibition of OII degradation by BQ may be due to $^1O_2$ as the main reactive species promoting the catalytic process. Furthermore, 30 mmol/L L-His and FFA exhibited a significant inhibitory impact on OII oxidation. L-His completely inhibited OII oxidation (Fig. S6 in Supporting information, $k_{30mmol/L,L\text{-}His} = 0.0006$ min^{-1}), demonstrating that $^1O_2$ was generated in the system, denoting the dominant reactive species for the degradation of OII. This phenomenon indicated that $^1O_2$ represented the dominant reactive species for OII degradation, followed by $^{\bullet}OH$, $SO_4^{\bullet-}$, and $O_2^{\bullet-}$.

$$HSO_5^- \rightarrow H^+ + SO_5^{2-} \quad (8)$$

$$HSO_5^- + SO_5^{2-} \rightarrow HSO_4^- + SO_4^{\bullet-} + {}^1O_2 \quad (9)$$

Electron spin-resonance (ESR) spectroscopy confirmed the presence of the active species in the GBO + PMS system using 5,5-dimethyl-1-pyrroline *N*-oxide (DMPO) and 2,2,6,6-tetramethyl-4-piperidone (TEMP) as spin-trapping agents, as shown in Figs. 3c-e. Fig. 3c illustrates the typical TEMP-$^1O_2$ spin adduct signal observed in the PMS-only and GBO + PMS systems, which was significantly enhanced in the GBO + PMS system. DMPO-$^{\bullet}OH$/$SO_4^{\bullet-}$ and DMPO–$O_2^{\bullet-}$ adduct signals were also observed after introducing DMPO to the PMS-only and GBO + PMS systems (Figs. 3d and e). Furthermore, all the samples showed similar species signals, while those at 10 min were stronger than at 5 min. The corresponding signals of the GBO + PMS system were distinctly stronger than in the PMS-only system, which might explain the enhanced PMS activation by the GBO catalyst.

GBO displayed excellent reusability for PMS activation and OII degradation in circumneutral pH conditions (initial pH 6.6). The OII degradation rate declined by only 3% after five consecutive reaction cycles (Fig. 3f), which was likely due to slight Mn leaching (<0.75 mg/L, Fe leaching cannot be detected) (Fig. S6c), as well as $Mn^{2+}/Mn^{3+}/Fe^{2+}$ oxidation.

The redox behavior of GBO in a mixed solution containing Na_2SO_4 and PMS was studied using cyclic voltammetry (CV). As shown in Fig. S7 (Supporting information), the anode and cathode peaks indicated that redox reactions had occurred on the surface of the catalyst [2,37,54]. The GBO corrosion potential was measured using Tafel polarization curves to further investigate the electron migration rate of GBO. Fig. S7b shows that the GBO exhibited a much higher corrosion current (3.83×10^{-3} A) than the previously reported catalyst. This implies that the GBO demonstrates a high electron transfer rate for superior catalytic capability [7,41].

As shown in Figs. 1c-e, the GBO surface redox reaction was verified *via* XPS. The peak intensity of the GBO–OII Mn(IV) species was noticeably lower than GBO (11.48%). Mn(III) exhibited a 9.82% increase, while Mn(II) was about 1.66% higher, confirming the conversion between the two Mn species on the GBO surface. Compared with the Fe species content at various valence levels before and after the reaction, Fe(III) exhibited a 16.06% decrease since it was partially reduced to Fe(II). The results confirmed the presence of the Fe(III) and Fe(II) cycles during the reaction. Moreover, the relative content of O_α decreased from 64.80% to 53.97%, O_β increased from 16.99% to 24.07%, and O_γ increased by about 3.75%. These findings can be attributed to the formation of higher lattice oxygen levels on the GBO surface, while the surface −OH and H_2O participated in the redox reaction of the Mn and Fe species.

Based on active radical identification and XPS analysis, a plausible GBO + PMS activation mechanism for OII degradation was proposed. HSO_5^- was attached to the GBO surface in an OII solution. Manganese and iron oxides with different metal center valences (Mn(II), Mn(III), Mn(IV), Fe(II), and Fe(III)) on the GBO surface acted as active HSO_5^- reaction sites to generate $SO_4^{\bullet-}$ (Eqs. 10–16) [1,26,46] and $^{\bullet}OH$ (Eqs. 16 and 17) [7,47]. Moreover, Mn(IV) reacted with Fe(II) to produce Mn(III) and Fe(III) (Eq. 18) [26]. The $SO_4^{\bullet-}$ further reacted with H_2O (or OH^-) to produce $^{\bullet}OH$, based on Eqs. 19 and 20 [1,55]. Furthermore, the HSO_5^- decomposed to

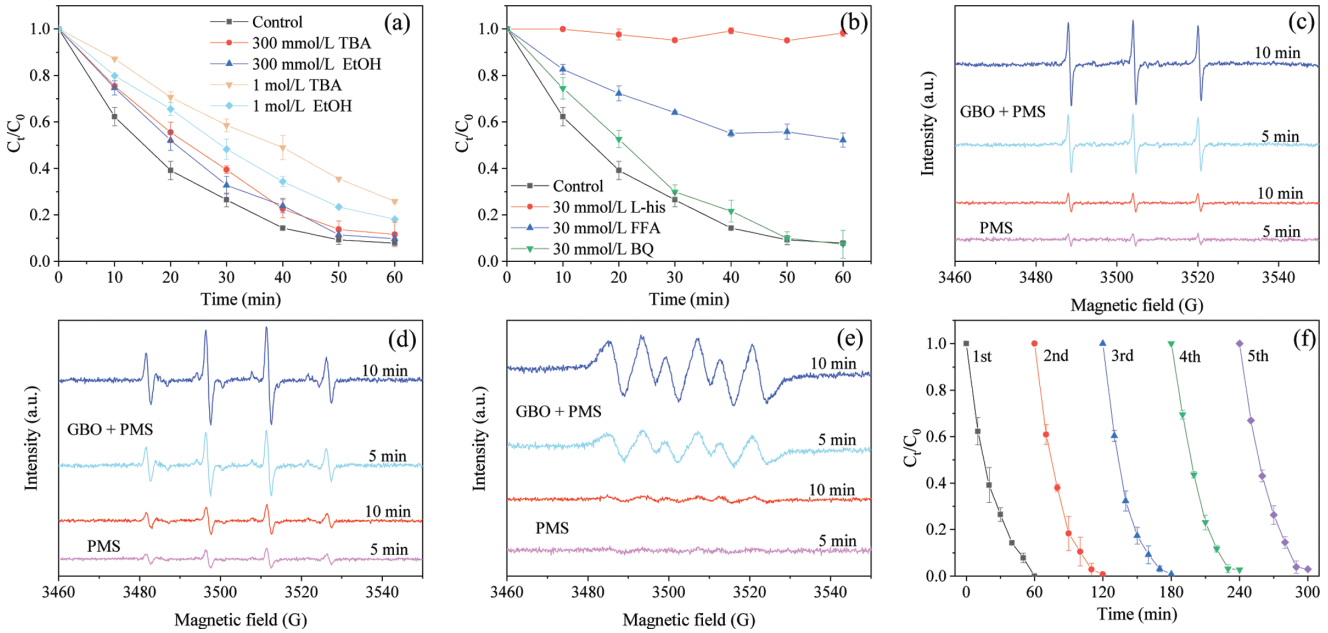

Fig. 3. (a) The quenching effect of $^{\bullet}OH$ and $SO_4^{\bullet-}$ on OII degradation. (b) The quenching effect of $^1O_2$ and $O_2^{\bullet-}$ on OII degradation. The ESR spectra of the (c) TEMP-$^1O_2$, (d) DMPO-$^{\bullet}OH/SO_4^{\bullet-}$ and (e) DMPO–$O_2^{\bullet-}$ adducts formed in PMS-only and GBO + PMS systems after 5 min and 10 min. (f) A recycling study of OII degradation. Conditions: C_0 = 20 mg/L, M_{GBO} = 0.97 g/L, M_{PMS} = 0.14 mmol/L, pH 6.6, T = 25 °C.

form $SO_4^{\bullet-}$, $^1O_2$, and SO_5^{2-} (Eqs. 8 and 9) [52,53]. The SO_5^{2-} reacted with H_2O to produce $O_2^{\bullet-}$ (Eq. 21) [32]. The $O_2^{\bullet-}$ and $SO_5^{\bullet-}$ further reacted with $^{\bullet}OH/H^+$ and H_2O to generate $^1O_2$ (Eqs. 22–24) [26,56].

$$\equiv Mn(IV) + HSO_5^- \rightarrow \equiv Mn(III) + SO_5^{\bullet-} + H^+ \quad (10)$$

$$\equiv Mn(III) + HSO_5^- \rightarrow \equiv Mn(II) + SO_5^{\bullet-} + H^+ \quad (11)$$

$$\equiv Mn(II) + HSO_5^- \rightarrow \equiv Mn(III) + SO_4^{\bullet-} + OH^- \quad (12)$$

$$\equiv Mn(III) + HSO_5^- \rightarrow \equiv Mn(IV) + SO_4^{\bullet-} + OH^- \quad (13)$$

$$\equiv Fe(III) + HSO_5^- \rightarrow \equiv Fe(II) + SO_5^{\bullet-} + H^+ \quad (14)$$

$$\equiv Fe(II) + HSO_5^- \rightarrow \equiv Fe(III) + SO_4^{\bullet-} + OH^- \quad (15)$$

$$\equiv Mn(IV) + HSO_5^- \rightarrow \equiv Mn(III) + SO_4^{\bullet-} + {}^{\bullet}OH \quad (16)$$

$$\equiv Mn(III) + HSO_5^- \rightarrow \equiv Mn(IV) + SO_4^{2-} + {}^{\bullet}OH \quad (17)$$

$$\equiv Mn(IV) + \equiv Fe(II) \rightarrow \equiv Mn(III) + \equiv Fe(III) \quad (18)$$

$$SO_4^{\bullet-} + H_2O \rightarrow H^+ + SO_4^{2-} + {}^{\bullet}OH \quad (19)$$

$$SO_4^{\bullet-} + OH^- \rightarrow SO_4^{2-} + {}^{\bullet}OH \quad (20)$$

$$SO_5^{2-} + H_2O \rightarrow O_2^{\bullet-} + SO_4^{2-} + H^+ \quad (21)$$

$$2SO_5^{\bullet-} + H_2O \rightarrow 1.5\ {}^1O_2 + SO_4^{2-} + 2HSO_4^- \quad (22)$$

$$O_2^{\bullet-} + {}^{\bullet}OH \rightarrow {}^1O_2 + OH^- \quad (23)$$

$$2O_2^{\bullet-} + 2H^+ \rightarrow {}^1O_2 + H_2O_2 \quad (24)$$

OII mineralization was evaluated to provide insight into the degradation of OII in the system. The total organic carbon (TOC) removal rate was 11.2% and 36.6% at 10 min and 60 min (Fig. S8 in Supporting information), respectively. The OII was partially removed from the system, of which a small fraction was completely mineralized. Therefore, the degradation and intermediate OII products may remain as residual substances. Gas chromatography mass spectrometry (GCMS) was used to analyze the reaction intermediates and elucidate the degradation pathway of OII in the GBO + PMS system. Table S3 (Supporting information) shows that twelve degradation intermediates were detected. The potential OII degradation pathways are proposed in Fig. S9 (Supporting information) according to the reaction mechanism and identified intermediates. The degradation process was initiated by N=N bond cleavage due to the oxidative attack of $^{\bullet}OH$, $SO_4^{\bullet-}$, and $O_2^{\bullet-}$ radicals, as well as $^1O_2$, leading to the formation of 1-amino-2-naphthol and sodium sulfanilamide [28,57–59]. The 1-amino-2-naphthol was oxidized to form 1,2-dihydroxynaphthalene and 1-methylnaphthalene [59], while sodium sulfanilamide oxidation resulted in toluene, *p*-xylene, and *p*-benzoquinone. All the intermediates were further oxidized and mineralized to CO_2, H_2O, NO_3^-, and SO_4^{2-} [7].

In summary, this work highlights the outstanding ability of GBO to catalyze PMS decomposition, removing 92.2% of OII within 60 min. An exceedingly low E_a level is achieved for OII degradation in the GBO + PMS system. The established GBO + PMS system shows significant potential for degrading OII in a broad pH range. $^1O_2$ is identified as the primary reactive species for OII degradation, followed by $^{\bullet}OH$, $SO_4^{\bullet-}$, and $O_2^{\bullet-}$. Moreover, the results indicate that the Mn and Fe species play a crucial role in catalytic activity, while GBO also exhibits excellent stability and reusability. This work provides a novel application approach for GBO as an efficient PMS activator and will be useful during the future design and fabrication of transition metal PMS catalysts.

Declaration of competing interest

The authors declare that they have no known competing financial interests or personal relationships that could have appeared to influence the work reported in this paper.

Acknowledgments

The authors acknowledge the funding support from Talent Introduction Program of Xihua University (No. Z202117). The authors would like to thank Shiyanjia Lab (www.shiyanjia.com) for the ESR analysis.

Supplementary materials

Supplementary material associated with this article can be found, in the online version, at doi:10.1016/j.cclet.2022.01.029.

References

[1] M.M. Mian, G. Liu, B. Fu, Y. Song, Appl. Catal. B: Environ. 255 (2019) 117765.
[2] Z. Dong, Q. Zhang, B.Y. Chen, J. Hong, Chem. Eng. J. 357 (2019) 337–347.
[3] C. Wang, J. Kang, P. Liang, et al., Environ. Sci.: Nano 4 (2017) 170–179.
[4] A. Sharma, J. Ahmad, S.J.S. Flora, Environ. Res. 167 (2018) 223–233.
[5] J. Wang, S. Wang, Chem. Eng. J. 411 (2021) 128392.
[6] W.D. Oh, Z. Dong, T.T. Lim, Appl. Catal. B: Environ. 194 (2016) 169–201.
[7] R. Yuan, Z. Jiang, Z. Wang, et al., J. Colloid Interface Sci. 571 (2020) 142–154.
[8] Y. Yang, G. Banerjee, G.W. Brudvig, et al., Environ. Sci. Technol. 52 (2018) 5911–5919.
[9] C. Chai, C. Fan, J. Liu, et al., J. Solid State Chem. 277 (2019) 466–474.
[10] M. Kohantorabi, G. Moussavi, S. Giannakis, Chem. Eng. J. 411 (2021) 127957.
[11] X. Duan, C. Su, J. Miao, et al., Appl. Catal. B: Environ. 220 (2018) 626–634.
[12] Y. He, J. Zhang, H. Zhou, et al., Chem. Eng. J. 380 (2020) 122568.
[13] Z. Wu, Y. Wang, Z. Xiong, et al., Appl. Catal. B: Environ. 277 (2020) 119136.
[14] X. Tian, P. Gao, Y. Nie, et al., Chem. Commun. 53 (2017) 6589–6592.
[15] Z. Zhao, J. Zhao, C. Yang, Chem. Eng. J. 327 (2017) 481–489.
[16] Z. Huang, C. Liu, X. Zhu, et al., Chem. Pap. 74 (2020) 641–650.
[17] Y.Y. Ahn, J. Choi, M. Kim, et al., Environ. Sci. Technol. 55 (2021) 5382–5392.
[18] R. Yin, W. Guo, H. Wang, et al., Chem. Eng. J. 335 (2018) 145–153.
[19] M. Kermani, M. Farzadkia, M. Morovati, et al., J. Environ. Manage. 266 (2020) 110616.
[20] Y. Qi, R. Qu, J. Liu, et al., Chemosphere 237 (2019) 124484.
[21] Q. Wang, P. Rao, G. Li, et al., Ecotoxicol. Environ. Saf. 187 (2020) 109779.
[22] L. Chen, X. Zuo, S. Yang, et al., Chem. Eng. J. 359 (2019) 373–384.
[23] C.X. Li, C.B. Chen, J.Y. Lu, et al., Chem. Eng. J. 337 (2018) 101–109.
[24] B. Huang, Z. Wu, H. Zhou, et al., J. Hazard. Mater. 412 (2021) 125253.
[25] X. Duan, H. Sun, Z. Shao, S. Wang, Appl. Catal. B: Environ. 224 (2018) 973–982.
[26] C. Lyu, D. He, Z. Mou, X. Yang, Sci. Total Environ. 693 (2019) 133589.
[27] G. Chen, X. Zhang, Y. Gao, et al., Sep. Purif. Technol. 213 (2019) 456–464.
[28] L. Hou, X. Li, Q. Yang, et al., Sci. Total Environ. 663 (2019) 453–464.
[29] X. Tian, L. Xiao, J. Colloid Interface Sci. 580 (2020) 803–813.
[30] J. Huang, Y. Dai, K. Singewald, et al., Chem. Eng. J. 370 (2019) 906–915.
[31] D. Wang, L. Wang, G. Liang, et al., ACS Nano 13 (2019) 10643–10652.
[32] H. Fu, P. Zhao, S. Xu, et al., Chem. Eng. J. 375 (2019) 121980.
[33] J. Du, J. Bao, Y. Liu, et al., Chem. Eng. J. 376 (2019) 119193.
[34] T. Yamashita, P. Hayes, Appl. Surf. Sci. 254 (2008) 2441–2449.
[35] X. Wang, X. Pu, Y. Yuan, et al., Chin. Chem. Lett. 31 (2020) 2634–2640.
[36] L. Liu, B. Wang, X. Yao, et al., Fuel 283 (2021) 119336.
[37] A. Khan, K. Zhang, A. Taraqqi-A-Kamal, et al., J. Colloid Interface Sci. 599 (2021) 805–818.
[38] Y. Zhao, H. An, J. Feng, et al., Environ. Sci. Technol. 53 (2019) 4500–4510.
[39] J. You, C. Zhang, Z. Wu, et al., Chem. Eng. J. 415 (2021) 128890.
[40] D. Zeng, Z. Dan, F. Qin, H. Chang, Mater. Chem. Phys. 242 (2020) 122307.
[41] Y. Li, J. Li, Y. Pan, et al., Chem. Eng. J. 384 (2020) 123361.
[42] A. Eslami, M. Hashemi, F. Ghanbari, J. Cleaner Prod. 195 (2018) 1389–1397.
[43] S. Zhu, X. Li, J. Kang, et al., Environ. Sci. Technol. 53 (2019) 307–315.
[44] M. Ahmadi, F. Ghanbari, Mater. Res. Bull. 111 (2019) 43–52.
[45] M. Ahmadi, F. Ghanbari, A. Alvarez, S.S. Martinez, Korean. J. Chem. Eng. 34 (2017) 2154–2161.
[46] Y.H. Huang, Y.F. Huang, C.I. Huang, C.Y. Chen, J. Hazard. Mater. 170 (2009) 1110–1118.
[47] Y. Wang, S. Indrawirawan, X. Duan, et al., Chem. Eng. J. 266 (2015) 12–20.
[48] Y. Feng, D. Wu, Y. Deng, et al., Environ. Sci. Technol. 50 (2016) 3119–3127.
[49] M. Huang, S. Peng, W. Xiang, et al., Chem. Eng. J. 429 (2022) 132372.
[50] J.C.E. Yang, Y. Lin, H.H. Peng, et al., Appl. Catal. B: Environ. 268 (2020) 118549.
[51] Z. Xiong, Y. Jiang, Z. Wu, et al., Chem. Eng. J. 421 (2021) 127863.
[52] J. Wang, S. Wang, Chem. Eng. J. 334 (2018) 1502–1517.
[53] Y. Zhou, J. Jiang, Y. Gao, et al., Environ. Sci. Technol. 49 (2015) 12941–12950.
[54] Y. Ren, L. Lin, J. Ma, et al., Appl. Catal. B: Environ. 165 (2015) 572–578.
[55] L. Zhu, Z. Shi, L. Deng, Y. Duan, Colloids Surf. A 609 (2021) 125637.
[56] J. Zhang, W. Zhao, S. Wu, et al., J. Hazard. Mater. 410 (2021) 124623.
[57] J. Wu, H. Zhang, J. Qiu, J. Hazard. Mater. 215-216 (2012) 138–145.
[58] S. Feng, B. Xiao, M. Wu, et al., Sep. Purif. Technol. 248 (2020) 117004.
[59] Y. Xu, X. Guo, F. Zha, et al., J. Environ. Manage. 253 (2020) 109695.